Ultrafast double-quantum-coherence spectroscopy of excitons with entangled photons

Marten Richter* and Shaul Mukamel
Department of Chemistry, University of California Irvine, Irvine, California 92697-2025, USA
(Received 10 May 2010; published 19 July 2010)

We calculate the four-wave-mixing signal of excitons generated at $\boldsymbol{k}_4 = \boldsymbol{k}_1 + \boldsymbol{k}_2 - \boldsymbol{k}_3$ by two pulsed entangled photon pairs $(\boldsymbol{k}_1, \boldsymbol{k}_2)$ and $(\boldsymbol{k}_3, \boldsymbol{k}_4)$, where all four modes are chronologically ordered. Entangled photons offer an unusual combination of bandwidths and temporal resolution not possible by classical beams. Contributions from different resonances can be selected by varying the parameters of the photon wave function. The signal scales linearly rather than quadratically with the laser field intensity, which allows performance of the measurements at low powers.

DOI: 10.1103/PhysRevA.82.013820 PACS number(s): 42.65.Re, 42.50.Dv, 33.80.Wz

I. INTRODUCTION

Since the introduction of entangled photon sources [1,2], they have become an important tool in imaging and fabrication of masks for semiconductors, where higher spatial resolutions using multiphoton absorption can be achieved at lower laser intensities [3,4]. The properties of entangled light sources of different types have been extensively studied. There are different types of entanglement [5–10]: two photons can be entangled by their polarization or by their correlations between different modes (often denoted frequency or temporal entanglement). Most effort so far has focused on the properties of the light [5,7,11–14]. In [4] and [15–17] entangled photons were used for spectroscopy and showed to reveal more information about the system than with similar setups which use classical beams.

An important aspect is the scaling of the signal with light intensities; classical $\chi^{(3)}$ signals scale quadratically with the intensity and, therefore, require a high intensity to be visible against lower order linear-scaling processes. $\chi^{(3)}$ signals with entangled photons scale linearly with the intensity [18,19]. These allow the use of low power for microscopy [3] and lithography [20] applications.

Time-domain two-dimensional (2D) spectroscopic techniques [21] provide a versatile tool for exploring the properties of excitonic systems such as photosynthetic aggregates [22,23] or coupled (hybrid) nanostructures to semiconductor quantum wells [24–27]. These techniques use short coherent pulses in comparison to the dephasing times of the system.

The wave function of entangled photons offers additional control parameters to the optical signals compared with classical fields. Two-photon absorption and its variation with the entanglement time were analyzed theoretically [28] and experimentally [4]. Additionally, it was theoretically shown that spectroscopic methods using entangled photons can show a high resolution along certain frequency axes [15,17], despite the broad frequency band caused by the intrinsic time ordering and time correlation of the entangled light source. These hybrid characteristics of frequency- and time-domain techniques are not possible with classical beams. Here we consider resonant pulsed measurements. An off-resonant configuration was theoretically studied in [17].

In this paper we focus on the double-quantum-coherence technique [29–32], which makes the energies of single and biexciton energies accessible and reveals the correlations between single and biexcitonic states. We show how pulsed entangled photons affect the two-photon resonances. Some bandwidth limitations of classical beams are removed and selectivity of quantum pathways is possible.

The paper is structured as follows: First, we introduce the model Hamiltonian for the excitonic system, then we present the general formula for two-photon absorption signals using closed time-loop diagrams. Then the pulse configuration used for the entangled photon coherence is introduced and the signal is calculated. Finally, the signal and possible ways of tuning the double-quantum-coherence spectra are discussed.

II. THE EXCITON MODEL

We consider a system described by the Frenkel exciton Hamiltonian:

$$H = H_0 + H', \tag{1}$$

$$H_0 = \hbar \sum_i \varepsilon_i B_i^\dagger B_i + \hbar \sum_{i \neq j} J_{ij} B_i^\dagger B_j + \hbar \sum_i \frac{\Delta_i}{2} B_i^\dagger B_i^\dagger B_i B_i, \tag{2}$$

$$H' = \hat{E}(t,\boldsymbol{r}) V^\dagger + \hat{E}^\dagger(t,\boldsymbol{r}) V, \tag{3}$$

$$V = \sum_i V_i^\dagger B_i^\dagger, \tag{4}$$

$$E = \frac{1}{\sqrt{2}} \sum_{kj} e_{\omega(\mathbf{k}_j)} a_j^\dagger(\boldsymbol{k}_j) e^{-\imath\omega t},$$

$$e_\omega = (\hbar\omega/\epsilon_0 V_Q)^{1/2}. \tag{5}$$

H_0 is the excitonic part and H' is the dipole interaction with the optical field in the rotating wave approximation. B_i is a bosonic excitonic operator at site i; this could be, for example, a pigment or a quantum dot, as in [33]. $a_j^\dagger$ and a_j are photon creation and annihilation operators, $\hat{E}$ is the electric field operator, and V_Q is the quantization volume. To describe two-level sites which cannot be doubly excited, we set $\Delta_i \to \infty$.

*marten.richter@tu-berlin.de; on leave from Institut für Theoretische Physik, Technische Universität Berlin, Berlin, Germany.

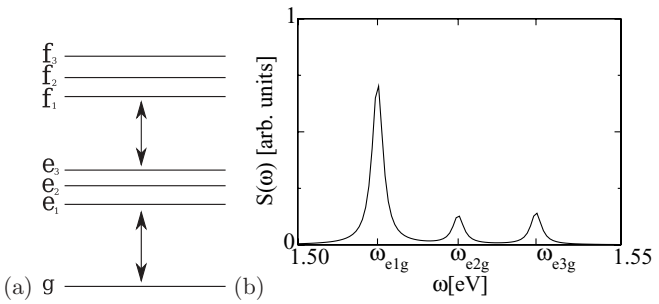

FIG. 1. (a) Level scheme of the excitonic model system made of three coupled two-level systems. (b) Absorption spectrum. The model parameters are $\varepsilon_1 = 1.518\,\text{eV}$, $\varepsilon_2 = 1.530\,\text{eV}$, and $\varepsilon_3 = 1.526\,\text{eV}$, $J_{12} = 10\,\text{meV}$, $J_{13} = 2\,\text{meV}$, and $J_{23} = 3\,\text{meV}$, and $V_1 = V_2 = V_3$.

The eigenstates of Eq. (2) form separated exciton bands. For our applications we need the lowest three: the ground state g, single-exciton states e, and double-exciton states f. The diagonalized Hamiltonian then assumes the form

$$H_0 = E_g|g\rangle\langle g| + \sum_e E_e|e\rangle\langle e| + \sum_f E_f|f\rangle\langle f|, \tag{6}$$

$$V^\dagger = \sum_e V_{ge}^*|e\rangle\langle g| + \sum_{ef} V_{ef}^*|f\rangle\langle e|. \tag{7}$$

The level scheme of the model of three coupled two-level systems used in our simulations together with a absorption spectrum is depicted in Fig. 1.

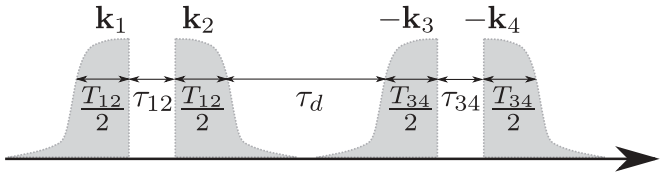

FIG. 2. Pulse configuration for the double-quantum-coherence signal.

III. THE DOUBLE-QUANTUM-COHERENCE SIGNAL

We assume four beams of two entangled photon pairs $(\boldsymbol{k}_1,\boldsymbol{k}_2)$ and $(\boldsymbol{k}_3,\boldsymbol{k}_4)$ with $\boldsymbol{k}_4 = \boldsymbol{k}_1 + \boldsymbol{k}_2 - \boldsymbol{k}_3$ (Fig. 2). The signal is defined as the change in the transmitted intensity in mode $\boldsymbol{k}_4$:

$$S = \int \frac{d}{dt}\langle \hat{E}_4^\dagger(t)\hat{E}_4(t)\rangle\, \mathrm{d}t. \tag{8}$$

The two entangled photon pairs are temporally well separated and $(\boldsymbol{k}_1,\boldsymbol{k}_2)$ comes before $(\boldsymbol{k}_3,\boldsymbol{k}_4)$. In addition, the two photons in each pair are time ordered; $\boldsymbol{k}_1$ comes before $\boldsymbol{k}_2$, and $\boldsymbol{k}_3$ before $\boldsymbol{k}_4$. We thus have a similar configuration to an impulsive experiment with four short, well-separated classical fields, we have a delay τ_{12} between the photons in the entangled pair $\boldsymbol{k}_1$ and $\boldsymbol{k}_2$ (τ_{34} for $\boldsymbol{k}_3$ and $\boldsymbol{k}_4$) and a delay $T_{12}/2 + \tau_d + T_{34}/2$ between the two photon pairs. The two entanglement times need to be included in this delay time to guarantee that $\boldsymbol{k}_1$ and $\boldsymbol{k}_2$ come before $\boldsymbol{k}_3$ and $\boldsymbol{k}_4$ for all $\tau_d > 0$.

The two contributions to the signal are depicted as closed time-loop diagrams in Fig. 3. The signal is given by

$$\begin{aligned} S(\Gamma) = -\frac{1}{\hbar^3}\mathrm{Re}\int_0^\infty \mathrm{d}s_1 \int_0^\infty \mathrm{d}s_2 \int_0^\infty \mathrm{d}s_3 \int_0^\infty \mathrm{d}s_4 [&-\langle\Psi|\hat{E}_3^\dagger(s_1+s_2+s_3-s_4)\hat{E}_4^\dagger(s_1+s_2+s_3)\hat{E}_2(s_1+s_2)\hat{E}_1(s_1)|\Psi\rangle \\ &\times\langle V^\dagger(s_1+s_2+s_3-s_4)V^\dagger(s_1+s_2+s_3)V(s_1+s_2)V(s_1)\rangle \\ &+\langle\Psi|\hat{E}_4^\dagger(s_1+s_2+s_3+s_4)\hat{E}_3^\dagger(s_1+s_2+s_3)\hat{E}_2(s_1+s_2)\hat{E}_1(s_1)|\Psi\rangle \\ &\times\langle V^\dagger(s_1+s_2+s_3+s_4)V^\dagger(s_1+s_2+s_3)V(s_1+s_2)V(s_1)\rangle]. \end{aligned} \tag{9}$$

It may be depicted by its variation with various parameters of the field wave function. These are denoted collectively as Γ. Various choices of Γ lead to different types of 2D signals. These are specified in the following sections [see Eqs. (25) and (26)].

Before inserting Eq. (19) into Eq. (9), we change the integration variables to $\tau_1 = s_2$, $t_2 = s_1 + s_2$, $\tau_3 = s_4$, and $t = s_1 + s_2 + s_3$ for (i) or $t = s_1 + s_2 + s_3 + s_4$ for (ii) (see Fig. 3). This transforms the times along the loop in Fig. 3 to real times in the pulse configuration (Fig. 2). Here s and t are interaction times of the second photon in the first or the second pair, respectively; τ_1 and τ_3 are the time differences between the interaction of the first and that of the second photon in the

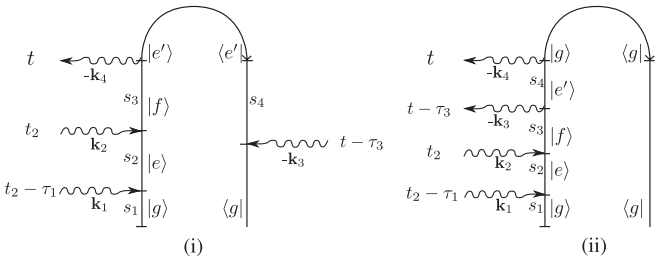

FIG. 3. Pathways contributing to the double-quantum-coherence signal at $\boldsymbol{k}_4 = \boldsymbol{k}_1 + \boldsymbol{k}_2 - \boldsymbol{k}_3$ (for diagram rules, see [34] and [35]). s_i are the time intervals along the loop, whereas t, t_2, $t - \tau_3$, and $t_2 - \tau_1$ are real physical time variables.

first or second pair, respectively. The photon configuration is depicted in Fig. 2. τ_{12}, τ_{34}, and T are positive. Making use of the factorization $|\Psi\rangle = |\Psi_{12}\rangle|\Psi_{34}\rangle$, we get

$$S(\Gamma) = S_i(\Gamma) + S_{ii}(\Gamma), \tag{10}$$

$$\begin{aligned} S_i(\Gamma) = \frac{1}{\hbar^3}\mathrm{Re}\int_{-\infty}^{\infty}\mathrm{d}t\int_0^{\infty}\mathrm{d}\tau_3\int_{-\infty}^{\infty}\mathrm{d}t_2\int_0^{\infty}\mathrm{d}\tau_1 \\ \times\sum_{ee'f} V_{e'f}V_{ge'}V_{ef}^*V_{ge}^* e^{-\imath\xi_{fe'}\tau_3-\imath\xi_{fg}(t-\tau_3-t_2)-\imath\xi_{eg}\tau_1} \\ \times\langle\Psi_{12}|\hat{E}_1(t_2-\tau_1)\hat{E}_2(t_2)|\Psi_{12}\rangle \\ \times\langle\Psi_{34}|\hat{E}_3^{\dagger}(t-\tau_3)\hat{E}_4^{\dagger}(t)|\Psi_{34}\rangle, \end{aligned} \tag{11}$$

$$\begin{aligned} S_{ii}(\Gamma) = -\frac{1}{\hbar^3}\mathrm{Re}\int_{-\infty}^{\infty}\mathrm{d}t\int_0^{\infty}\mathrm{d}\tau_3\int_{-\infty}^{\infty}\mathrm{d}t_2\int_0^{\infty}\mathrm{d}\tau_1 \\ \times\sum_{ee'f} V_{ge'}V_{e'f}V_{ef}^*V_{ge}^* e^{-\imath\xi_{e'g}\tau_3-\imath\xi_{fg}(t-\tau_3-t_2)-\imath\xi_{eg}\tau_1} \\ \times\langle\Psi_{12}|\hat{E}_1(t_2-\tau_1)\hat{E}_2(t_2)|\Psi_{12}\rangle \\ \times\langle\Psi_{34}|\hat{E}_3^{\dagger}(t-\tau_3)\hat{E}_4^{\dagger}(t)|\Psi_{34}\rangle. \end{aligned} \tag{12}$$

We have introduced the complex frequency variables $\xi_{ij} = \omega_{ij} + \imath\gamma_{ij}$, where $\omega_{ij} = \varepsilon_i - \varepsilon_j$ are the transition frequencies and γ_{ij} are the dephasing rates. In our calculations we set $\gamma_{ij} = \gamma = 1$ meV.

IV. THE FIELD CORRELATION FUNCTION FOR ENTANGLED PHOTON PAIRS

We assume the following wave function for the entangled photon pair i and j [5]:

$$|\Psi(\tau)\rangle = |0\rangle + \sum_{k_i,k_j} f(\boldsymbol{k}_i,\boldsymbol{k}_j)a_i^{\dagger}(\boldsymbol{k}_i)a_j^{\dagger}(\boldsymbol{k}_j)|0\rangle \tag{13}$$

where $|0\rangle$ is the vacuum state of the radiation field. The photons generated by a pump pulse are emitted in two different directions and polarizations in type II parametric downconversion, where one photon is generated in H and one in V polarization. Furthermore, we assume an entangled photon pair generated with a phase-matching condition as described in Ref. [5]. Then $f(\boldsymbol{k}_i,\boldsymbol{k}_j)$ has the form

$$\begin{aligned} f(\boldsymbol{k}_i,\boldsymbol{k}_j) = g\hat{u}\big((\omega(\boldsymbol{k}_j)-\omega(\boldsymbol{k}_i)\big)/2)e^{-\imath[\omega(\boldsymbol{k}_i)+\omega(\boldsymbol{k}_j)]\hat{\tau}_{ij}} \\ \times e^{-\imath[\omega(\boldsymbol{k}_j)]\tau_{ij}}E^P\big(\omega(\boldsymbol{k}_i)+\omega(\boldsymbol{k}_j)-\Omega_P\big), \end{aligned} \tag{14}$$

$$\hat{u}(\omega) = e^{\imath T_{ij}\omega/2}\mathrm{sinc}(T_{ij}\omega/2), \tag{15}$$

where $E^P(\cdots)$ is the envelope, and Ω_p the central frequency of the pump pulse used to generate the pairs.

The entanglement times T_{ij} characterize the temporal correlation of the entangled photons. They are determined by the generating crystal length. The correlation functions of the entangled fields read [5]

$$\begin{aligned} \langle\Psi|\hat{E}_1(t_1)\hat{E}_2(t_2)|\Psi\rangle = V_0^{12}e^{-i\frac{\Omega_p}{2}(t_1+t_2-\tau_{12})}u_{12}(t_2-t_1-\tau_{12}) \\ \times E_p\left(\frac{t_1+t_2-\tau_{12}}{2}\right), \end{aligned} \tag{16}$$

$$\begin{aligned} \langle\Psi|\hat{E}_3^{\dagger}(t_3)\hat{E}_4^{\dagger}(t_4)|\Psi\rangle = V_0^{34}e^{-i\frac{\Omega_p}{2}(t_3+t_4-\tau_{34}-2\Delta t_{34})}u_{34}(t_4-t_3-\tau_{34}) \\ \times E_p^*\left(\frac{t_3+t_4-\tau_{34}}{2}-\Delta t_{34}\right), \end{aligned} \tag{17}$$

$$\Delta t_{34} = \tau_{12} + T_{12}/2 + \tau_d + T_{34}/2, \tag{18}$$

$$u_{ij}(t) = \begin{cases} \frac{1}{T_{ij}}, & 0 < t < T_{ij}, \\ 0, & \text{otherwise}, \end{cases}$$

$$E_p(t) = \exp[-t^2/(2\sigma^2)]. \tag{19}$$

$E_p(t)$ is the temporal envelope function of the pump pulse which generates the entangled photon pair. The correlation function Eq. (16) is depicted in Fig. 4(a); it is finite only above the diagonal line at $t_2 = t_1 + \tau$, reflecting the time ordering between $\boldsymbol{k}_1$ and $\boldsymbol{k}_2$ and between $\boldsymbol{k}_3$ and $\boldsymbol{k}_4$. The product $E_1(t_1)E_2(t_2)$ for the classical field is shown for comparison in Fig. 4(b). A variation in the delay time τ_{12} will shift the entire correlation function of photons $\boldsymbol{k}_1$ and $\boldsymbol{k}_2$ along the τ_{12} axis. The correlation function is determined along the diagonal axis by the envelope E_p and on the perpendicular axis by u_{12}. In the frequency domain [Fig. 4(c)], temporal entanglement is shown by the diagonal shape of the correlation function.

V. SIMULATED TWO-DIMENSIONAL SIGNALS

By inserting Eq. (19) into Eq. (9) and carrying out all integrations, assuming that $\gamma\,\sigma \ll 1$, we arrive at the final expression for the two contributions to the signal:

$$\begin{aligned} S_i(\Gamma) = \frac{1}{\hbar^3}\mathrm{Re}\sum_{ee'f} V_{e'f}V_{ge'}V_{ef}^*V_{ge}^*V_0^{12}V_0^{34}|E^p(\omega_{fg}-\Omega_p)|^2 \\ \times e^{-\imath\xi_{eg}\tau_{12}}e^{-\imath\xi_{fe'}\tau_{34}}e^{-\imath\xi_{fg}\tau_d} \\ \times\frac{[e^{\imath(\omega_{fg}/2-\xi_{eg})T_{12}}-1]e^{-\imath\xi_{fg}T_{12}/2}}{\imath(\omega_{fg}/2-\xi_{eg})T_{12}} \\ \times\frac{[e^{\imath(\omega_{fg}/2-\xi_{fe'})T_{34}}-1]e^{-\imath\xi_{fg}T_{34}/2}}{\imath(\omega_{fg}/2-\xi_{fe'})T_{34}}, \end{aligned} \tag{20}$$

$$\begin{aligned} S_{ii}(\Gamma) = \frac{1}{\hbar^3}\mathrm{Re}\sum_{ee'f} V_{ge'}V_{e'f}V_{ef}^*V_{ge}^*V_0^{12}V_0^{34}|E^p(\omega_{fg}-\Omega_p)|^2 \\ \times e^{-\imath\xi_{eg}\tau_{12}}e^{-\imath\xi_{e'g}\tau_{34}}e^{-\imath\xi_{fg}\tau_d} \\ \times\frac{[e^{\imath(\omega_{fg}/2-\xi_{eg}]T_{12}}-1]e^{-\imath\xi_{fg}T_{12}/2}}{\imath(\omega_{fg}/2-\xi_{eg})T_{12}} \\ \times\frac{[e^{\imath(\omega_{fg}/2-\xi_{e'g}]T_{34}}-1]e^{-\imath\xi_{fg}T_{34}/2}}{\imath(\omega_{fg}/2-\xi_{e'g})T_{34}}, \end{aligned} \tag{21}$$

$$|E^p(\omega)|^2 = \exp(-\sigma^2\omega^2/2). \tag{22}$$

The parameter Γ now includes the delay times τ_{12}, τ_{34}, and τ_d and the entanglement times T_{12} and T_{34}.

For comparison, we present the same signal obtained with four impulsive classical pulses with envelopes $E^j(\omega)$, $j = 1,\ldots,4$ and carrier frequency Ω_p^0 [33]:

$$\begin{aligned} S_i^{(3)} = \frac{1}{\hbar^3}\mathrm{Re}\sum_{ee'f} V_{e'f}V_{ge'}V_{ef}^*V_{ge}^*E^{4*}\big(\omega_{fe'}-\Omega_p^0\big) \\ \times E^{3*}\big(\omega_{e'g}-\Omega_p^0\big)E^2\big(\omega_{fe}-\Omega_p^0\big)E^1\big(\omega_{eg}-\Omega_p^0\big) \\ \times e^{-\imath\xi_{eg}\tau_{12}}e^{-\imath\xi_{fe'}\tau_{34}}e^{-\imath\xi_{fg}\tau_d}, \end{aligned} \tag{23}$$

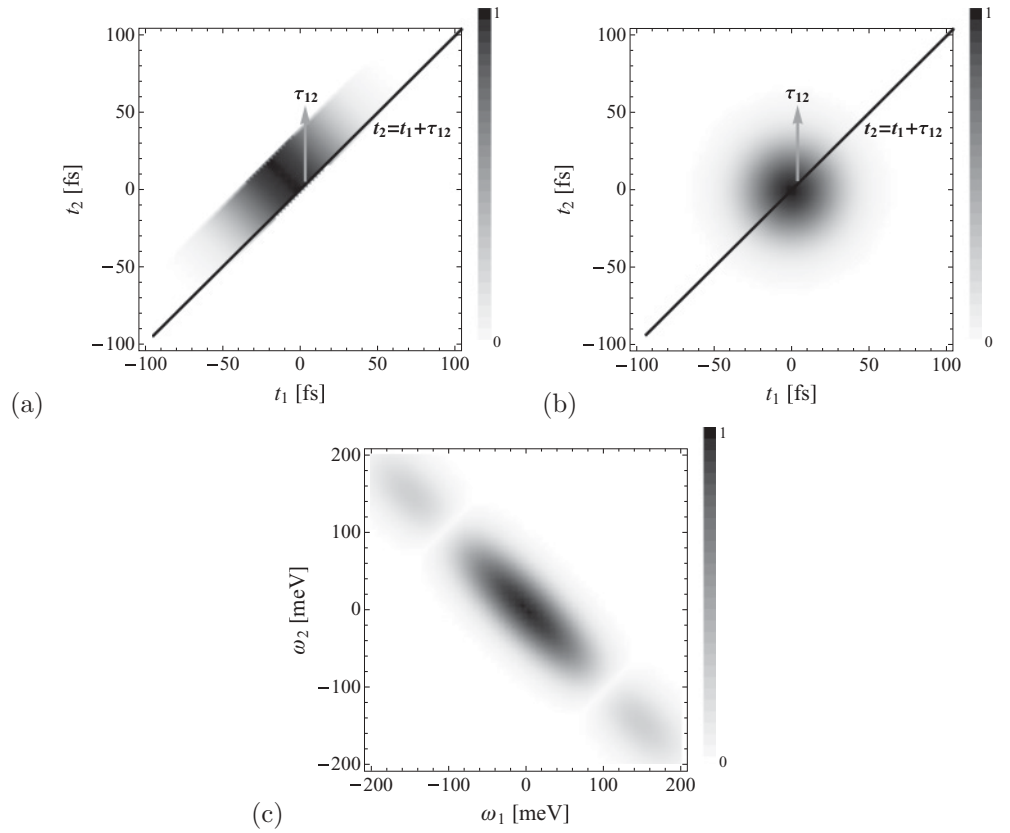

FIG. 4. (a) Entangled photon correlation function $\langle E_1(t_1)E(t_2)\rangle$ for a pulsed entangled photon pair, Eq. (19) ($\tau_{12}=0$, $T_{12}=40$ fs, $\sigma=20$ fs). (b) Analog plot for two classical impulsive pulses. (c) Fourier transform of (a).

$$S_{ii}^{(3)} = \frac{1}{\hbar^3}\mathrm{Re}\sum_{ee'f} V_{ge'}V_{e'f}V_{ef}^{*}V_{ge}^{*}E^{4*}\left(\omega_{e'g}-\Omega_p^0\right) \times E^{3*}\left(\omega_{fe'}-\Omega_p^0\right)E^{2}\left(\omega_{fe}-\Omega_p^0\right)E^{1}\left(\omega_{eg}-\Omega_p^0\right) \times e^{-\imath\xi_{eg}\tau_{12}}e^{-\imath\xi_{e'g}\tau_{34}}e^{-\imath\xi_{fg}\tau_d}. \quad (24)$$

With Eqs. (20) and (21), we can compare the entangled and classical double-quantum-coherence signals. We first note that Eq. (20) scales linearly with the pump intensity, in contrast to quadratic scaling for the classical case, Eq. (23). In the classical case the signal is limited by the bandwidths of the four pulses [cf. Eqs. (23) and (24)], which control the four transitions (ω_{eg}, ω_{fe}, $\omega_{e'g}$, $\omega_{fe'}$) in the two photon transitions inside the pulse bandwidth [33]. In Eq. (20) bandwidth limitations of the envelopes are only imposed through the bandwidth of entangled photon pair $E^p(\cdot)$, and the limitation is only imposed on the two-photon transition ω_{fg}, leading to a much broader bandwidth for the ω_{eg} and ω_{fe} transitions, provided the ω_{fg} transition is within the generating pump-pulse bandwidth.

We illustrate this effect in Fig. 5 for the following 2D signal:

$$S(\Omega_{12},\Omega_{34}) = \int_0^\infty \mathrm{d}\tau_{12}\int_0^\infty \mathrm{d}\tau_{34}S(\tau_{12},\tau_{34})e^{-\imath\tau_{12}\Omega_{12}-\imath\tau_{34}\Omega_{34}}, \quad (25)$$

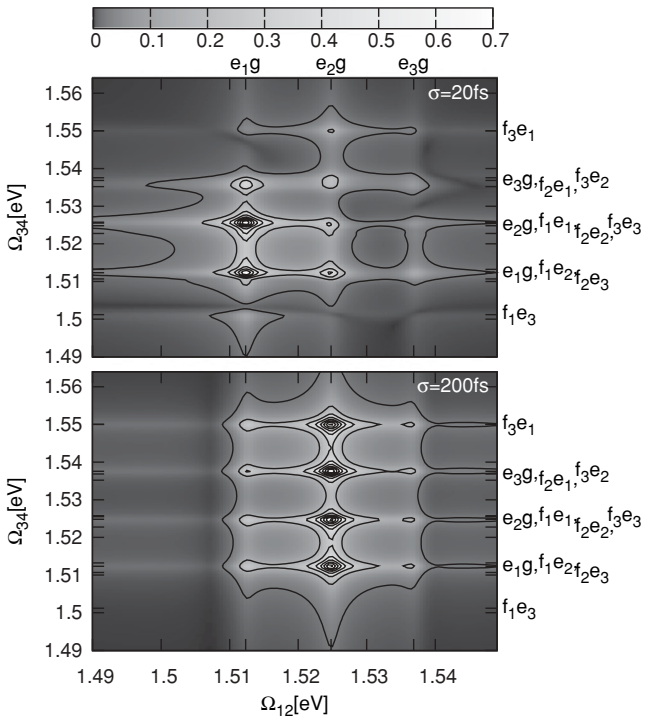

FIG. 5. Two-dimensional signal, Eq. (25) (absolute value), showing correlation plots for $T_{12}=T_{34}=20$ fs, $\Omega_P=3.0621$ eV, with different pump durations σ as indicated. The bottom plot is multiplied by a factor of 6.

ω_{eg} resonances are seen along Ω_{12}, and ω_{eg} and ω_{fe} along the Ω_{34} axis. As the bandwidth is reduced in Fig. 5(b), we only get contributions from the biexciton resonant with the generating pump. This results in four identical patterns along the Ω_{12} axis. All peaks are connected to the same biexciton states. More precisely we get four contributions along the Ω_{12} axis connected to the transitions $\omega_{f_3e_1}$, $\omega_{f_3e_2}$, overlapping with ω_{e_3g}, ω_{e_2g}, overlapping with $\omega_{f_3e_3}$ and ω_{e_1g}. The remaining transitions are not affected by the reduced pump bandwidth. Here the pump-pulse narrow bandwidth can be used to select contributions in the spectra connected to a specific biexciton state.

In Fig. 6 we display a different signal:

$$S(\Omega_{12},\Omega_d) = \int_0^\infty d\tau_{12} \int_0^\infty d\tau_d S(\tau_{12},\tau_d) e^{-\imath\tau_{12}\Omega_{12}-\imath\tau_d\Omega_d}. \quad (26)$$

This shows ω_{eg} resonances along Ω_{12}, and ω_{fg} on Ω_d. It is similar to Fig. 5 except that here we see the single excitonic contributions ω_{e_1g}, ω_{e_2g}, and ω_{e_3g} to the selected biexciton f_3 along one row.

Bandwidth limitations on the single excitonic transitions ω_{eg} and ω_{fe} are only imposed indirectly by the factors in Eqs. (20) and (21) which depend on the entanglement times T_{12} and T_{34}. These become largest for $\omega_{fg} = 2\omega_{fe}$.

The factors in Eqs. (20) and (21) which depend on the entanglement times T_{ij} contain an interference term of the form $[e^{\imath(\omega-\gamma)T_{ij}} - 1]$, where ω is a material frequency. (This effect was described for two-photon absorption in Ref. [28].) Some resonances will interfere destructively at certain values of the entanglement time which matches the period of ω. We can therefore use the entanglement times to control these

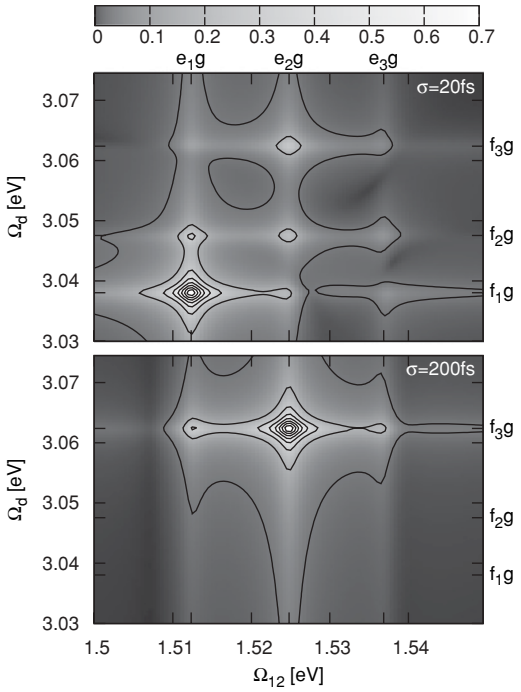

FIG. 6. Two-dimensional signal, Eq. (26) (absolute value), showing correlation plots for $T_{12} = T_{34} = 20$ fs, $\Omega_P = 3.0621$ eV, with different pump durations σ. The bottom plot is multiplied by a factor of 100.

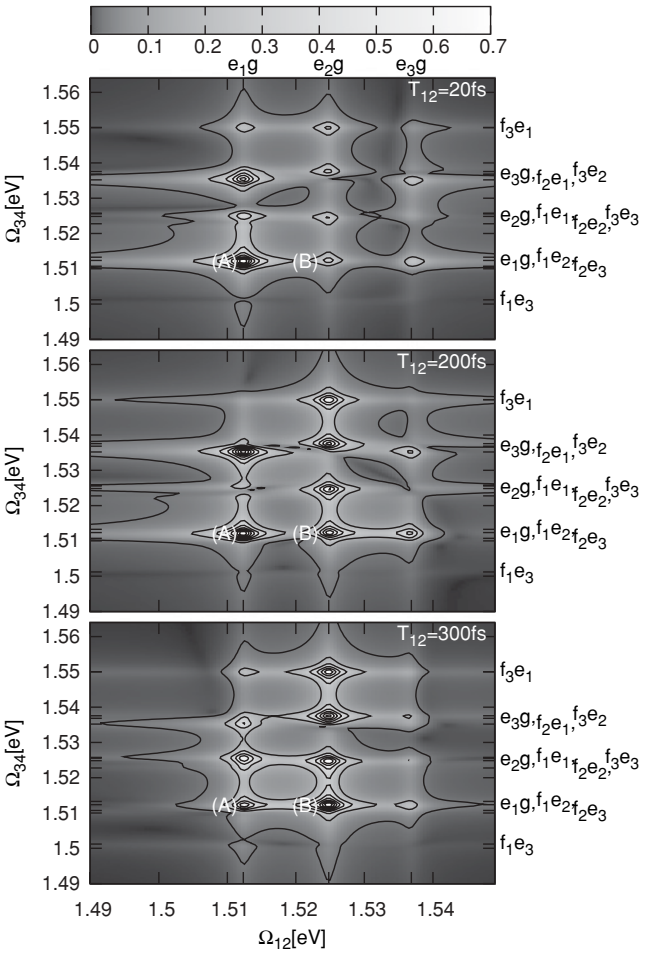

FIG. 7. Two-dimensional signal, Eq. (25) (absolute value), showing correlation plots for $T_{34} = 20$ fs, $\Omega_P = 3.11$ eV, $\sigma = 1/(20$ fs), and different values of T_{12} as indicated. Plots are multiplied by a factor of 1 (top), 3.5 (middle), and 6.0 (bottom).

resonances. Since the frequencies ω do not match the resonances on the plotted axis, two spectrally close features can be separated by using shots at different entanglement times. This holds only as long the entanglement times are shorter than the dephasing time, since otherwise the signal will be very weak. The frequencies ω can be $\omega_{fg}/2 - \omega_{eg}$ or $\omega_{fg}/2 - \omega_{fe}$ (which differs from the first frequency only by a sign) for different combinations of the states e, e', and f. By varying T_{12}, we expect an oscillation of the magnitudes of resonances with different frequencies. This is exactly what we see in Fig. 7. We focus on resonances A and B. At $T_{12} = 20$ fs, peak A is much stronger than peak B, however, as T_{12} increases the peak height of A is much more similar to that of B at $T_{12} = 200$ fs, while at $T_{12} = 300$ fs B is finally stronger than A. (Note that all plots are normalized to the strongest resonance.) The reason for this is that both peaks undergo a sinclike oscillation with a different frequency, it gives us additional control over the spectrum. This can also be true for two partially overlapping resonances in some cases, and the entanglement time provides a tool for dissecting them. The same effect is seen for other resonances, which clearly show that the oscillation frequency is characteristic for each peak. We can analyze the peak oscillations in more detail: Peak A is connected to ω_{e_1g} on

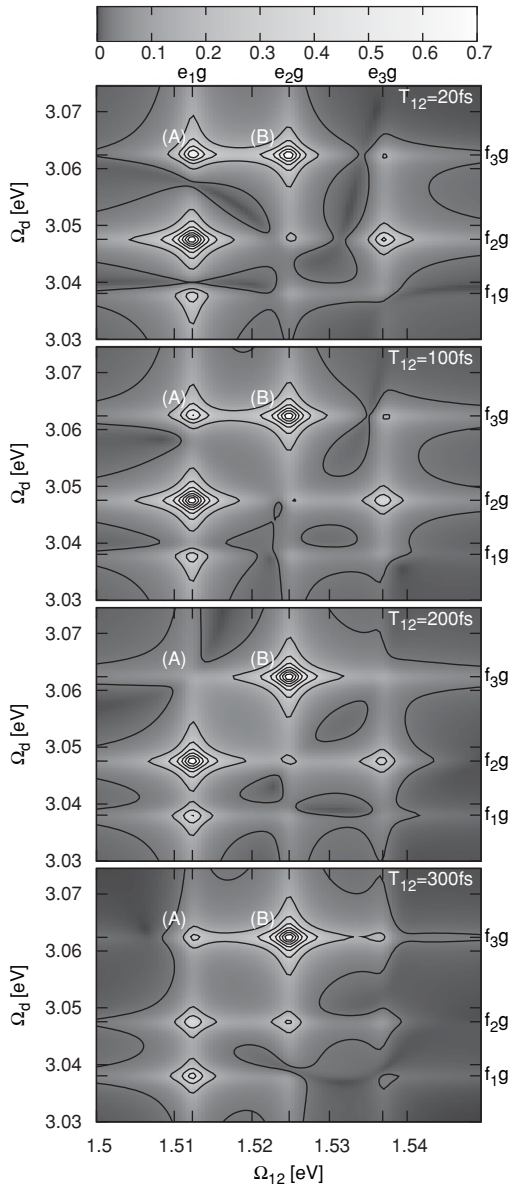

FIG. 8. Two-dimensional signal, Eq. (26) (absolute value), showing correlation plots for $T_{34} = 20$ fs, $\Omega_P = 3.11$ eV, $\sigma = 20$ fs, and T_{12} values as indicated. Plots are multiplied by a factor of (from top to bottom) 1, 1.3, 2, and 3.0.

the Ω_{12} axis and ω_{e_1g} on the other axis; thus in fact all three excitonic states contribute, and the oscillation of this peak should be a superposition of these three contributions at three different oscillation frequencies ($\omega_{f_ig}/2 - \omega_{e_1g}$). B consists of two peaks with ω_{e_2g} on the Ω_{12} axis and $\omega_{f_1e_2}$ or ω_{e_1g} on the Ω_{34} axis.[1] The part connected with ω_{e_1g} on Ω_{34} is similar to A connected to all three biexciton states and has parts oscillating at three frequencies $\omega_{f_ig}/2 - \omega_{e_2g}$; the part with ω_{e_1g} on Ω_{34} will oscillate only with $\omega_{f_1g}/2 - \omega_{e_2g}$. Note that the e state in the oscillation frequency is determined by the Ω_1 axis if we vary T_{12}; if we vary T_{34} instead, it is determined by the states assigned to the transitions on the Ω_{34} axis.

For the 2D signals in Fig. 8, resonance A can be assigned to ω_{e_1g} on the Ω_{12} axis and ω_{f3g} on the Ω_d axis, whereas resonance B is connected to ω_{e_2g} and ω_{f3g}. A has a strength similar to that of B at $T_{12} = 20$ fs; at $T_{12} = 200$ fs, A is much weaker than B, but A increases again at $T_{12} = 300$ fs. A oscillates at a frequency of $\omega_{f_3g}/2 - \omega_{e_1g}$, and B at $\omega_{f_3g}/2 - \omega_{e_2g}$. If T_{34} is varied instead of T_{12}, the oscillation frequency will only be connected to ω_{f_ig} on the Ω_d axis; each peak will then be a superposition of oscillating contributions connected to different values of ω_{e_ig}. But a Fourier transform over T_{34} at a given point like A will separate the different contributions to this peak.

VI. CONCLUSION

Double-quantum-coherence 2D spectroscopy of excitons with entangled photon pairs has been presented. Compared to classical beams the technique offers improved intensity scaling, relaxed laser bandwidth requirements, and additional control parameters for the signal.

ACKNOWLEDGMENTS

This research was supported by the National Science Foundation (Grant No. CHE-0745892) and the National Institutes of Health (Grant No. GM-59230). This support is gratefully acknowledged. M.R. gratefully acknowledges support from the Alexander-von-Humboldt Foundation through the Feodor Lynen program.

[1] Actually there is a third contribution from $\omega_{f_2e_3}$ on the Ω_{34} axis, but this has a smaller dipole moment.

[1] Y. H. Shih, A. V. Sergienko, M. H. Rubin, T. E. Kiess, and C. O. Alley, Phys. Rev. A **50**, 23 (1994).
[2] A. Pe'er, B. Dayan, A. A. Friesem, and Y. Silberberg, Phys. Rev. Lett. **94**, 073601 (2005).
[3] M. Teich and B. Saleh, US Patent 5796477 (1998).
[4] D. I. Lee and T. Goodson III, J. Phys. Chem. B **110**, 25582 (2006).
[5] T. E. Keller and M. H. Rubin, Phys. Rev. A **56**, 1534 (1997).
[6] J. Brendel, N. Gisin, W. Tittel, and H. Zbinden, Phys. Rev. Lett. **82**, 2594 (1999).
[7] Y. Nambu, K. Usami, Y. Tsuda, K. Matsumoto, and K. Nakamura, Phys. Rev. A **66**, 033816 (2002).
[8] K. Edamatsu, G. Oohata, R. Shimizu, and T. Itoh, Nature **431**, 167 (2004).
[9] N. H. Akopian, N. Lindner, E. Poem, Y. Berlatzky, J. Avron, D. Gershoni, B. D. Gerardot, and P. M. Petroff, Phys. Rev. Lett. **96**, 130501 (2006).
[10] A. Carmele, F. Milde, M.-R. Dachner, M. B. Harouni, R. Roknizadeh, M. Richter, and A. Knorr, Phys. Rev. B **81**, 195319 (2010).

[11] Y.-H. Kim, V. Berardi, M. V. Chekhova, A. Garuccio, and Y. Shih, Phys. Rev. A **62**, 043820 (2000).
[12] M. B. Nasr, G. D. Giuseppe, B. E. Saleh, A. V. Sergienko, and M. C. Teich, Opt. Commun. **246**, 521 (2005).
[13] M. V. Fedorov, M. A. Efremov, P. A. Volkov, E. V. Moreva, S. S. Straupe, and S. P. Kulik, Phys. Rev. A **77**, 032336 (2008).
[14] Y. M. Mikhailova, P. A. Volkov, and M. V. Fedorov, Phys. Rev. A **78**, 062327 (2008).
[15] B. E. A. Saleh, B. M. Jost, H.-B. Fei, and M. C. Teich, Phys. Rev. Lett. **80**, 3483 (1998).
[16] M. R. Harpham, O. Suezer, C.-Q. Ma, P. Baeuerle, and I. Goodson, Theodore, J. Am. Chem. Soc. **131**, 973 (2009).
[17] O. Roslyak and S. Mukamel, Phys. Rev. A **79**, 063409 (2009).
[18] S. Friberg, C. Hong, and L. Mandel, Opt. Commun. **54**, 311 (1985).
[19] J. Javanainen and P. L. Gould, Phys. Rev. A **41**, 5088 (1990).
[20] A. N. Boto, P. Kok, D. S. Abrams, S. L. Braunstein, C. P. Williams, and J. P. Dowling, Phys. Rev. Lett. **85**, 2733 (2000).
[21] S. Mukamel, Annu. Rev. Phys. Chem. **51**, 691 (2000).
[22] G. S. Engel, T. R. Calhoun, E. L. Read, T.-K. Ahn, T. Mancal, Y.-C. Cheng, R. E. Blankenship, and G. R. Fleming, Nature **446**, 782 (2007).
[23] D. Abramavicius, D. V. Voronine, and S. Mukamel, Proc. Natl. Acad. Sci. USA **105**, 8525 (2008).
[24] T. Zhang, I. Kuznetsova, T. Meier, X. Li, R. P. Mirin, P. Thomas, and S. T. Cundiff, Proc. Natl. Acad. Sci. USA **104**, 14227 (2007).
[25] L. Yang, T. Zhang, A. D. Bristow, S. T. Cundiff, and S. Mukamel, J. Chem. Phys. **129**, 234711 (2008).
[26] B. Pasenow, H. Duc, T. Meier, and S. Koch, Solid State Commun. **145**, 61 (2008).
[27] M. Vogel, A. Vagov, V. M. Axt, A. Seilmeier, and T. Kuhn, Phys. Rev. B **80**, 155310 (2009).
[28] H.-B. Fei, B. M. Jost, S. Popescu, B. E. A. Saleh, and M. C. Teich, Phys. Rev. Lett. **78**, 1679 (1997).
[29] S. Mukamel, R. Oszwaldowski, and L. Yang, J. Chem. Phys. **127**, 221105 (2007).
[30] L. Yang and S. Mukamel, Phys. Rev. B **77**, 075335 (2008).
[31] J. Kim, S. Mukamel, and G. D. Scholes, Acc. Chem. Res. **42**, 1375 (2009).
[32] B. Palmieri, D. Abramavicius, and S. Mukamel, J. Chem. Phys. **130**, 204512 (2009).
[33] D. Abramavicius, B. Palmieri, D. V. Voronine, F. Sanda, and S. Mukamel, Chem. Rev. **109**, 2350 (2009).
[34] C. A. Marx, U. Harbola, and S. Mukamel, Phys. Rev. A **77**, 022110 (2008).
[35] S. Mukamel and S. Rahav, Adv. At. Mol. Opt. Phys. (in press, 2010).